Variable Mixing Nozzle Design with Slotted Vortex Generators for Jet Noise Reduction

Jonathan M. Burt[1]
NASA Glenn Research Center, Cleveland, Ohio 44135

A new variable geometry turbofan nozzle concept is presented with the dual goals of airport noise reduction and high propulsive efficiency at cruise, while employing only a single moving part. The nozzle utilizes a number of curved vanes to function as vortex generators (VGs) during takeoff and initial climb. Streamwise vortices provide an increase in mixing between the jet and external stream, with a resulting decrease in high frequency noise generation and a noise source distribution which is more amenable to airframe-based shielding. Unlike conventional VGs, the vanes are positioned without transverse incidence, and a pressure difference across the surface of each vane is created via an adjacent slot. During high altitude flight, when nozzle efficiency concerns outweigh any preference for jet noise reduction, all slots may be closed through rotation of a slotted ring inside the nozzle. RANS-based numerical analysis is performed to calculate propulsive metrics, determine noise source characteristics and understand various design parameter sensitivities. A new formulation is developed to approximately correct computed noise intensities for any throttle adjustments required to maintain takeoff thrust, and a rough estimate of shielding effectiveness is proposed by means of integration over a spatially distributed noise source. A total of 19 different nozzle geometries are considered in the present study. Results indicate significant noise benefits at takeoff, including a 2 kHz fly-over noise reduction of roughly 2-3 dB, while allowing for less than 15% of the net thrust reduction at supersonic cruise calculated for a fixed-penetration chevron nozzle.

I. Introduction

Despite considerable advances in jet noise mitigation over the past several decades, jet noise from turbofan engines during takeoff and initial climb remains a dominant contributor to airport noise. In addition to increases in turbofan bypass ratio on commercial jet aircraft – with corresponding reductions in exhaust speed, turbulence and acoustic source intensity – a number of different strategies have been investigated for reducing jet noise in order to address community noise concerns and to comply with airport noise regulations. Community noise standards and noise regulations are particularly difficult obstacles in the development of commercial supersonic transport, and airport noise can be viewed as one of the primary challenges (along with emissions, fuel consumption and sonic boom) to viable commercial supersonic aircraft design. Jet noise from supersonic aircraft is especially problematic due to factors including the need for low bypass ratio turbofan engines to reduce sonic boom and improve supersonic propulsive efficiency, high takeoff speeds in comparison to subsonic aircraft, and comparatively high drag under takeoff conditions. Taken together, these characteristics tend to produce impermissible levels of jet noise at takeoff, and may require aggressive jet noise reduction strategies to satisfy existing noise standards.

The airport noise problem for supersonic commercial aircraft has helped motivate a large number of experimental, computational and analytical studies into jet noise reduction. Strategies that have been considered include various types of multi-stream nozzles, thermal acoustic shields,[1] mixer-ejector nozzles,[2-4] chevrons and other mixing enhancement devices, and propulsion-airframe integration concepts involving over-wing or over-tail engine placement.[5] Although considerable acoustic benefits have been realized with nearly all of these strategies, few have demonstrated additional characteristics that are important for practical application to commercial aircraft propulsion systems. In particular, a practical noise reduction strategy should be low weight, mechanically simple, and have little impact on propulsive or aerodynamic efficiency during cruise or other high altitude flight phases when aircraft noise

[1]Research Engineer, Propulsion Systems Analysis Branch, AIAA Associate Fellow.

is not a significant concern. Moreover, the noise reduction provided must be strong enough such that, at takeoff, a significant reduction of objectionable frequency noise is retained after consideration of any required increase in throttle to compensate for propulsive losses.

Two jet noise reduction strategies which have shown promise in meeting at least some of the above characteristics are the mixer-ejector nozzle and over-wing/over-tail engine configurations. In theory the two ideas work very differently, as the mixer-ejector has historically been proposed to reduce jet noise by entraining low speed atmospheric flow in order to reduce nozzle exit velocity and thereby decrease external mixing layer velocity gradients. However, in practice both approaches utilize mechanical shielding, by either the mixer-ejector shroud or airframe components, to block direct radiation of jet noise to a farfield observer. It follows that for either noise reduction strategy, effectiveness tends to improve through enhanced mixing in the vicinity of the primary nozzle exit. As nearfield mixing increases between primary and secondary/atmospheric streams, high frequency noise production is increased in the primary nozzle exit region where mechanical shielding prevents radiation into the acoustic farfield, while high frequency noise production is reduced further downstream.

The desired mixing enhancement between the engine exhaust and surrounding atmospheric flow may be accomplished by means of lobed mixers, chevrons,[2] pulsed jets, ramps,[6] or vane-type vortex generators (VGs).[7-9] Both chevrons and lobed mixer configurations are known to permit rapid mixing at takeoff, with chevrons generally providing an advantage in reduced viscous losses while lobed mixers allow greater penetration and mixed flow uniformity. Other mixing enhancement devices listed above have been subject to very little detailed study under relevant conditions. However, all may present design challenges associated with cruise performance, weight and/or added variable geometry complexity. More specifically, these devices may be employed in a fixed geometry configuration, where mixing enhancement at high speed and high altitude conditions leads to thrust losses with no corresponding desired acoustic benefits. Alternatively, such devices may use variable geometry (e.g. variable penetration chevrons) at the expense of increased weight, complexity, cost and maintenance requirements. For example, VG pitch can be varied in order to align VGs with the jet axis during high speed flight, and thereby eliminate trailing vortices. However, around 30 to 60 moving parts would likely be required in a variable pitch VG nozzle, following a rough estimation based on existing designs of variable inlet guide vanes. It should be noted that minimization of variable geometry elements is an especially important consideration in nozzle design, due to factors including possible exposure to high temperature exhaust flow, other thermal and mechanical stresses, and thermal expansion at rotating joints or linkages.

The present work focuses on a new type of nozzle configuration utilizing vane-type VGs, with the intention of balancing mixing efficacy against other desired characteristics as mentioned above. One concern of particular interest here is mechanical simplicity for variable geometry; in other words, the goal is to minimize the number and complexity of moving parts while avoiding significant thrust reduction during high speed flight. With this concern in mind, the proposed configuration uses a single moving part to transition between takeoff and cruise geometries. The nozzle employs a number of vanes, distributed circumferentially across the internal nozzle surface just upstream of the nozzle lip, to function as VGs during takeoff and initial climb. The vanes are positioned without transverse incidence, in contrast to conventional VGs, and a pressure difference across the surface of each vane is created by allowing flow to circulate through an adjacent slot. During cruise and transonic operation, when nozzle efficiency concerns outweigh any preference for jet noise reduction, all slots may be closed through rotation of a slotted ring which is located either inside the nozzle or (as may be preferable for smaller scale applications) along the external nozzle surface. This ring, which is centered along the jet axis, includes slots that can be aligned with the slots along the nozzle inner wall to enable trailing vortex generation around the jet mixing layer, or can instead be misaligned via rotation to eliminate trailing vortices.

The configuration described above is assessed in this work through a numerical design space exploration, where the practicality, drawbacks and relative benefits of the proposed concept are evaluated for a representative turbofan engine exhaust flow on a commercial supersonic transport. Reynolds averaged Navier-Stokes (RANS) based computational fluid dynamics (CFD) calculations are combined with acoustic analogy post-processing to determine takeoff noise characteristics – either with and without shielding provided through over-wing or over-tail engine placement – as well as propulsive characteristics at both takeoff and supersonic cruise conditions. The paper is structured as follows: In Section II initial design choices and design space restrictions are outlined, and RANS simulation setup and boundary conditions are described. This section also includes discussion of gridding methodology, along with modeling assumptions and simplifications. In Section III, detailed flowfield and acoustic source distribution results are presented for a baseline slotted VG nozzle case, and various flowfield structures and mixing enhancement mechanisms are identified. Next, in Section IV, a new dimensionless integral parameter is

proposed to quantify the axial variation in turbulent kinetic energy (TKE) that is assumed to function as a primary noise source, and values of this parameter are plotted for an initial set of nozzle geometries. Plots are also provided for integrated acoustic quantities, and results are presented for propulsive efficiency metrics. Section V includes sensitivity analysis results for several design parameters, in an effort to determine dominant and/or favorable design characteristics for the slotted VG nozzle concept. In Section VI results are provided from an investigation into noise directivity for a subset of considered nozzle geometries. Section VII describes the impact of an approximate throttle correction, derived in an appendix, which is used to adjust noise estimates for an increase in takeoff throttle. This throttle increase is required to compensate for thrust losses associated with nozzle noise reduction. In Section VIII results are presented from an assessment of nozzle performance at supersonic cruise conditions. Finally, Section IX includes a summary of study findings and conclusions.

II. Nozzle Geometry Characteristics, Flow Conditions and Simulation Setup

As outlined above, the basis of the proposed nozzle configuration is in the use of fixed VG vanes aligned with the jet axis, along with slots on one side of each VG to create a pathway between internal/exhaust and external/atmospheric streams. For unchoked or subsonic exit conditions on a convergent nozzle, the static pressure will typically be greater along the inner edge of a slot than along the outer edge, leading to outward flow through the slot. This outward flow creates a pressure imbalance between opposite VG surfaces, and the difference in pressures produces a trailing vortex. Additional trailing vortices are generated along the outer edges of each slot, due to the interaction between the external stream and the flow through the slot, and these slot vortices interact with each other and with VG vortices to further enhance nearfield mixing between the internal and external streams. In nozzle design, particular emphasis should be placed on exploiting interactions between trailing vortices from adjacent vortex generators, as favorable interactions should allow for alternating inward and outward flowing regions along the mixing layer that tend to promote rapid mixing.[10] It should be noted that vortex generator design requirements for jet mixing are distinct from those associated with boundary layer energization (as on aircraft wings) to delay stall or prevent separation.[9,11] In particular, for effective jet mixing enhancement, the vane height should be significantly greater than the boundary layer thickness, and ideal scale, inclination and aspect ratio values may be very different.

In order to reduce dimensionality in a design space exploration for the proposed nozzle concept, some design choices based on preliminary numerical analysis (not presented here) and existing VG geometries were used to exclude certain design parameters from the present study. These choices include the following: First, VGs are not positioned along the nozzle outer surface due to a finding of near-negligible impact on jet mixing enhancement for conditions of interest. Second, the downstream edge of each slot – assuming that the slot does not extend all the way to the nozzle lip – is positioned sufficiently downstream of the VG trailing edge to avoid significant impact on the VG surface pressure distribution. Next, low aspect ratio VGs are used to position most of the slot-side VG surface close to the slot opening, where the local pressure difference between opposite VG surfaces will be comparatively large. This should allow for an increase in trailing vortex strength for a given VG wetted area. Lastly, to reduce thrust loss at takeoff, a shallow extrusion angle (fixed here at 15°) and circular planform shape are used along the front and back surfaces of each slot. A few other beneficial design choices identified in preliminary work are used here to inform nozzle design, and are investigated in a subsequent sensitivity analysis study as part of this work. One such additional design choice is the positioning of adjacent VGs and slots in symmetric pairs, in order to utilize vortex interactions for increased radial velocities across the mixing layer. Another of these choices is to curve each VG inward around the slot, or to create overhang, in order to minimize the mass flow rate through the slot for a given difference in average surface pressure between opposite sides of the neighboring VG. These design choices are illustrated in Fig. 1, which shows VG/slot pairs over part of a convergent nozzle for which the flow is directed from left to right.

The conditions of interest, including freestream conditions for initial climb and various engine parameters, are taken in part from engine data for conceptual design of a supersonic commercial aircraft propulsion system, and from a recent study for a proposed mixer-ejector/thermal acoustic shield configuration.[12] A generic low bypass ratio turbofan engine is considered, with a nozzle exit inner diameter of 0.89 m and a nozzle exit Mach number of approximately 0.9. For RANS analysis, freestream conditions (altitude = 1000 ft, T_∞ = 281.7 K, P_∞ = 0.964 atm, M_∞ = 0.3) are imposed along a planar inflow boundary located 0.59 m upstream of the nozzle lip. A nozzle pressure ratio of 2.17 and nozzle temperature ratio of 1.91 are used to set inflow boundary conditions for the internal flowpath along this same plane.

Figure 2 shows case geometries considered in an initial assessment of the slotted VG nozzle concept. These included the following: (1) a baseline convergent reference nozzle, which is axisymmetric and lacks any VGs or slots; (2) a nozzle with slots and curved VGs as in Fig. 1; (3) a nozzle with slots and flat VGs; (4) a nozzle that includes

slots but lacks VGs; (5) a nozzle without slots that includes flat 7.6×7.6 cm VGs which are set at 15° incidence to the jet axis; and (6) a chevron nozzle with 14 chevrons of length 10.2 cm and 20° penetration. All nozzles with VGs and/or slots have 18 of each arranged in equally spaced symmetric pairs. Slots are approximately 2.5 cm wide by 15.2 cm long, with an extrusion angle of 15°. Aside from those in case (5), all VGs have planform dimensions of 3.8×15.2 cm, for an aspect ratio of 1/4. For expected ease of manufacturing, VGs are modeled as plates of constant 0.5 cm thickness (equal to that of the nozzle lip) with an approximately circular rounded leading edge and a flat trailing edge.

All nozzle geometries, as shown in Fig. 2, are created using the CATIA software package then imported into the Pointwise gridding tool for surface and volume grid generation. Figure 3 shows a cutout view of surface and interior domains that bound various blocks in the Pointwise grid for the baseline geometry. The grid consists of one large unstructured block, along with several structured blocks positioned around the jet, as has been found in earlier work to significantly reduce numerical diffusion and dissipation effects within the mixing layer.[13] Cell stretching is employed in the axial direction within structured blocks, while Pointwise anisotropic cell layer growth ("T-Rex") routines are used in boundary layer regions to enforce a RANS accuracy criterion that $y^+ < 1$ along viscous wall boundaries. Additional cell stretching routines are used to reduce wall boundary face dimensions in the edge-normal direction around leading and trailing edge surfaces. RANS simulations are performed using the FUN3D code developed at NASA Langley Research Center, with second order point-implicit calculations that utilize local time stepping, the LDFSS flux splitting scheme, and the two-equation SST turbulence model of Menter with vorticity source terms.[14] The flow is approximated as single species calorically perfect gas, and adiabatic wall boundaries are assumed.

The mSrc code of Bridges[15] is used to post-process FUN3D results for determination of noise source distributions as functions of the local turbulent kinetic energy (TKE) and turbulent dissipation rate. An acoustic analogy relation with empirically derived scaling coefficients is employed in mSrc to estimate source densities with rough directivity considerations. Major approximations and potential error sources include a lack of Green's function modeling for sound propagation; no direct calculation of shielding, reflection or atmospheric attenuation effects; a lack of RANS consideration for large-scale turbulent structures that may be dominant contributors to low frequency jet noise; and various other simplifying assumptions and parameter calibrations that underly the SST turbulence model. Given these approximations and assumptions, it follows that computed acoustic quantities should generally be interpreted in a relative (not absolute) sense, for evaluation of design sensitivities and identification of trends.

III. Flowfield Characteristics

Case 2, as described above and illustrated in Figs. 1 and 2, is used throughout this section as a representative case to examine flowfield properties and structures. Figure 3 shows selected flowfield results from this case. TKE contours are displayed along the *x*-*z* plane and along several *x*-normal planes, and iso-contour surfaces of constant vorticity *x*-component values are overlaid. As expected, iso-contour surfaces show trailing vortices with opposite vorticity located downstream of adjacent and opposite vortex generators. Larger iso-contour surface structures – corresponding to increased vortex circulation – are located downstream of vortex generators along the inner nozzle wall, as results from the fact that considerably higher speed flow surrounds vortex generators on the inner wall than on the outer wall. Trends in the TKE distribution, as observed in Fig. 4, include a gradual outward spread in the mixing layer, and a reduction in azimuthal variation in TKE with downstream distance. In correlating trends between TKE and vorticity, it is interesting to note that azimuthal maxima in TKE occur around vortex interaction regions where the flow tends to circulate outward from the jet into the surrounding ambient flow, whereas inward-flowing regions within the mixing layer tend to exhibit local minima in TKE.

Figure 4 shows Mach contours and streamlines along the centerline plane, with additional lines (in purple) to denote sonic conditions. A weak Mach disk is observed in this figure just downstream of the nozzle exit, and slightly under-expanded nozzle exit conditions are indicated by divergent streamlines around the lip. Supersonic conditions are found throughout much of the jet core, as well as in portions of the outward flow through the slots.

In Fig. 5, velocity vectors are plotted along a transverse (*x*-normal) plane at a distance of one-half exit inner diameter downstream of the nozzle lip ($x/D_{exit} = ½$), with vector lengths proportional to velocity magnitude in the *y*-*z* plane and coloring based on the local radial flux of total enthalpy. The figure also includes iso-contour lines for TKE. The total enthalpy flux can be viewed as an indication of how much energy is available for conversion into TKE through coherent inward or outward streams that impinge on or cross the mixing layer; positive and negative flux values correspond to radially outward and inward streams, respectively. As observed through trends in velocity, trailing vortices are centered around the spanwise outer edges of VGs along the inner nozzle wall, and outer streamwise

vortex pairs are generated by interactions between the slot flow and external flow. Each co-rotating slot vortex (where the term "co-rotating" is used here to denote a vortex circulating in the same direction as the adjacent VG vortex) is pushed radially outward by a stream generated from interaction between the adjacent VG vortex and the counter-rotating slot vortex. Meanwhile, the interaction between neighboring counter-rotating slot vortices creates a radially inward-directed stream that impinges on the mixing layer, while an outward stream generated in the jet by the interaction of neighboring VG vortices impinges on the same portion of the mixing layer from the opposite direction. A local maximum in TKE is found in the vicinity of the mixing layer impingement region, indicating a likely increase in noise source intensity. Text overlaid on Fig. 5 should help to clarify the locations of flowfield structures and mixing enhancement mechanisms.

Figures 6 and 7 show, respectively, contours of TKE and x-directed vorticity along nine transverse planes located between the nozzle exit and an axial distance of two exit inner diameters downstream. Color blanking is used in Fig. 6 for values below 500 m^2/s^2 in order to more clearly present vortex roll-up other trends around the outer edges of the mixing layer. A comparison of the two figures shows the rapid evolution of vortex structures with downstream distance. As described above in the discussion of Fig. 5, a counter-rotating slot vortex interacts with each VG vortex to push a corresponding co-rotating slot vortex radially outward and away from the mixing layer. A mushroom-shaped pattern then emerges in TKE contours as the co-rotating slot vortex rolls up and diffuses into the surrounding external stream. As expected, the mixing layer is found to diffuse both outward and inward toward the jet axis, while vortex break-up is largely completed within the small axial distance represented in these plots.

In Fig. 8, contours of normalized pressure are shown over a portion of the nozzle surface. Pressure values are observed here to be considerably higher along the inner edge of each slot than along the outer edge, allowing for outward flow through the slot which in turn reduces the pressure on the slot-side surface of an adjacent VG. The resulting pressure imbalance across the VG leads to trailing vortex generation at the VG outer edge. Note the increase in pressure along the slot-side VG surface in the vicinity of the VG trailing edge. This is attributed to compression around the back (forward-facing) surface of the slot, and indicates a strong sensitivity in VG surface pressure distribution to the axial distance between the VG trailing edge and the downstream edge of the slot.

Contours of source density, as calculated in mSrc at frequencies of 2 kHz and 4 kHz, are plotted in Figs. 9. Slices are displayed at transverse planes defined by varying x/D_{exit} in increments of ½, with color blanking applied to values below 62 dB. Iso-contour surfaces at 70 dB are also shown in the figures. Following mSrc documention,[15] the source density $r_f(x, y, z)$ can be interpreted as the approximate contribution, per unit volume, of noise at a given location (x, y, z) and frequency f to sound intensity $s_f(R)$ for a farfield observer at a 90° polar angle and distance R,

$$s_f(R) = 10 \log_{10} \left[\frac{0.00320}{R^2} \iiint_{\infty} 10^{\left[\frac{1}{10} r_f(x,y,z)\right]} dx dy dz \right] \tag{1}$$

where R is in units of m, and both r_f and s_f are in dB. The source density r_f is computed in mSrc, through a semi-empirical acoustic analogy formulation, as a function of TKE and the local turbulent dissipation rate. As observed in Figs. 9, the 4 kHz noise source has an increased concentration around the upstream portion of the jet, whereas the 2 kHz noise source tends to persist further downstream. Consistent with trends in the TKE distribution, the noise source is generally focused in portions of the flowfield where vortex interactions generate streams that impinge on the mixing layer.

IV. Comparison of Integrated Quantities

For quantitative assessment of mixing enhancement based on RANS simulation results, and for comparison between cases 1-6 displayed in Fig. 2, some systematic measurement of relative mixing rates is desired. To evaluate axial variation in mixing rate from results of a single-species RANS simulation, the TKE production rate is found to be a potentially effective metric to evaluate turbulent mixing. (Other integrated flowfield quantities, including the x-derivatives of jet mass flow rate and entropy flow rate, were found in this work to be far more sensitive to numerical errors.) The planar integral of TKE flux, or TKE flow rate, should tend to increase with downstream distance within several exit diameters of the nozzle lip where TKE is produced in the mixing layer much faster than TKE is lost to turbulent dissipation. The rate of increase in the TKE flux planar integral, or equivalently the axial derivative of the TKE flow rate, should be highest in the area of strongest mixing within a short distance of the nozzle lip. Moreover, in comparing TKE production at a given x-location among various nozzle geometries, it is expected that higher rates

of increase will correspond to geometries for which mixing rates are comparatively high. It follows that jet mixing rates can be quantified, at least in a relative sense, by computing x-derivatives of the TKE flow rate.

A nondimensional parameter based on TKE is defined as follows:

$$P_{TKE}(x) \equiv \frac{1}{\dot{H}_{exit}} \frac{d}{d(x/D_{exit})} \iint_{\infty} [\rho v_x TKE] dydz = \frac{D_{exit}}{\dot{H}_{exit}} \iint_{\infty} \frac{d}{dx} [\rho v_x TKE] dydz \tag{2}$$

where the total enthalpy flow rate $\dot{H}_{exit}$ for uniform flow across the nozzle exit area is given by

$$\dot{H}_{exit} = \frac{1}{8} \pi D_{exit}^2 v_{x,exit} \left(\frac{2\gamma}{\gamma - 1} p_{exit} + \rho_{exit} v_{x,exit}^2 \right) \tag{3}$$

and where the normalization density ρ_{exit}, velocity $v_{x,exit}$ and pressure p_{exit} are taken from RANS output quantities at the nozzle exit center, as calculated for the reference axisymmetric nozzle case.

In Fig. 10 the normalized TKE flow rate derivative P_{TKE} is plotted for all six nozzle geometries shown in Fig. 2. Relative to the reference nozzle case (1), trends in P_{TKE} indicate increase mixing for $x/D_{exit} < 1$ and generally reduced mixing further downstream for geometries (2-5) that include VGs and/or slots. Large differences in P_{TKE} for the chevron nozzle case (6), relative to all other cases, may be attributed to the presence of stronger vortex-mixing layer interactions within a short distance of the nozzle, as well as an increase in downstream turbulent dissipation. Note that the influence of turbulent dissipation on the local energy balance outweighs that of shear-induced turbulence production where $P_{TKE} < 0$ for the chevron nozzle case.

In Fig. 11 the source density cross stream integral (SDCSI) is plotted for the reference nozzle and slotted curved VG nozzle (cases 1 and 2, respectively, in Fig. 2) at six different frequencies between 250 Hz and 8 kHz. The SDCSI, denoted here as ψ_f, is computed by integrating source density r_f over a transverse plane. With proper linear weighting for ψ_f and r_f which are both expressed in dB, it follows that

$$\psi_f(x) = 10 \log_{10} \left[\iint_{\infty} 10^{\left[\frac{1}{10} r_f(x,y,z)\right]} dydz \right] \tag{4}$$

This parameter may be used to characterize the downstream extent of noise generation at various frequencies. For both cases in Fig. 11, a tendency for broader distributions of noise at lower frequencies is observed, as expected. At distances $x/D_{exit} < 1$, Fig. 11 shows an increase in planar source intensity at all considered frequencies for the slotted VG case (2), whereas this case is found to consistently generate less noise than the reference nozzle case (1) at $x/D_{exit} > 2$.

An additional measure of noise intensity is provided through axial integration of the SDCSI ψ_f. More specifically, ψ_f may be integrated over the interval $[x, \infty)$ to estimate the total cumulative noise intensity at some frequency f to a farfield observer at a 90º polar angle, in the presence of mechanical shielding that extends a distance x downstream of the nozzle lip. This shielding could be provided, for example, by the horizontal tail in an over-tail engine configuration, or alternatively by a mixer-ejector shroud. The cumulative intensity, denoted by φ_f, is given in dB using the expression

$$\varphi_f(x) \equiv 10 \log_{10} \left[\int_x^{\infty} 10^{\left[\frac{1}{10} \psi_f(x)\right]} dx \right] \tag{5}$$

Cumulative intensities for all six nozzles shown in Fig. 2 are plotted at six different frequencies in Fig. 12. Important trends for all six cases in Fig. 12 include a consistent reduction in φ_f with increasing frequency, and a tendency for the slope magnitude – indicating the degree of upstream noise source concentration – to increase with frequency. Several other trends observed in the figure are strongly dependent on frequency and/or nozzle geometry; these trends are more easily viewed separately for individual frequencies, as presented in Figs. 13.

Fig. 13 (a) shows cumulative intensity variation $\varphi_f(x)$ for all six nozzles at 1 kHz. All curves in the figure are nearly horizontal for $x/D_{exit} < 0.5$, which indicates that shielding lengths less than $0.5D_{exit}$ would likely have negligible

impact on 1 kHz jet noise intensity for a farfield observer at a 90º polar angle. At $x/D_{exit} = 0$, significant reductions in cumulative intensity are found for all enhanced mixing (slot/VG and chevron) nozzle configurations relative to the axisymmetric reference nozzle (case 1). This suggests that, at 1 kHz, effective noise reduction may be accomplished through nozzle geometry modifications, even in the absence of shielding. Such a finding is consistent with experimental data[16] showing noise reduction at lower frequencies may be accomplished through breakup of large-scale turbulent eddies by streamwise vortices. In comparison to the reference nozzle (case 1), the greatest noise reduction at both $x/D_{exit} = 0$ and 1 is observed for the chevron nozzle (case 6), with 0.3-0.4 dB lower source intensity than either the curved (2) or flat (3) slotted VG nozzle cases. Note that, for clarity, a vertical line is included in the figure at $x/D_{exit} = 1$, representing a rough upper limit for practical shielding lengths. The two slotted VG nozzles both provide around 2 dB of noise reduction at 1 kHz for $0 \leq x/D_{exit} \leq 1$.

Cumulative source intensities at 2 kHz are presented in Fig. 13 (b). Qualitatively similar trends are found in this figure as in Fig. 13 (a), including a near-zero slope for $x/D_{exit} < 0.5$ and unshielded ($x/D_{exit} = 0$) noise reduction for all mixing enhancement geometries relative to the reference nozzle. However, in contrast to 1 kHz, at 2 kHz and $0 \leq x/D_{exit} \leq 1$ the chevron and VG nozzle without slots (cases 6 and 5, respectively) are shown to be considerably less effective in reducing noise than either slotted VG nozzle. Furthermore, of the two slotted VG nozzles, the nozzle with curved VGs is found to be significantly more effective in reducing 2 kHz noise. Relative to the reference nozzle, the maximum cumulative 2 kHz noise reduction at both $x/D_{exit} = 0$ and $x/D_{exit} = 1$ is observed for case 2, with source intensity differences of 1.8 dB and 2.3 dB, respectively.

Cumulative source intensities at 4 kHz are plotted in Fig. 13 (c). At this frequency, the chevron nozzle and VG nozzle without slots are surprisingly shown to cause *increased* cumulative noise relative to the reference nozzle over the practical shielding range $0 \leq x/D_{exit} \leq 1$. As with 2 kHz, at 4 kHz the maximum cumulative noise reduction over $0 \leq x/D_{exit} \leq 1$is found for the slotted VG nozzle employing curved VGs (case 2); 4 kHz cumulative noise reduction for this nozzle is estimated as 0.8 dB at $x/D_{exit} = 0$ and 2.2 dB at $x/D_{exit} = 1$.

Any comparison of acoustic benefits and mixing effectiveness for various nozzle geometries should include consideration of associated thrust loss. This follows in part from the need to avoid significant performance penalties from propulsion system modifications intended to reduce noise, and in part from the fact that, in order to compensate for thrust loss while maintaining some desired speed and acceleration at takeoff, engine throttle settings will likely need to increase. Additional noise related to this higher throttle may offset any noise reduction for a given nozzle, and acoustic and mixing improvements must therefore be weighed very carefully against thrust decrements. Moreover, nozzle modifications may affect the mass flow rate through an unchoked nozzle (i.e. a nozzle with subsonic exit conditions) which could in turn affect engine component efficiencies, temperatures, emissions and/or desired control settings for the engine and inlet.

Various metrics for propulsive efficiency are presented in Table 1 for all six nozzle geometries. The gross thrust is computed here by integrating the axial momentum flux (based on relative pressure) over the nozzle inflow boundary, then subtracting drag contributions from VG slot and nozzle inner/outer surfaces. The net thrust is then determined by subtracting the product of freestream velocity and computed nozzle mass flow rate (i.e. ram drag) from gross thrust, while the gross thrust coefficient C_{FG} is found as the ratio of gross thrust to the product of the computed mass flow rate and the ideal exit velocity for isentropic expansion to the freestream pressure.

In the table, a thrust increase relative to the reference nozzle is shown for all three slotted nozzle cases; this increase is attributed to mass flow through the slots, which leads to increased mass flow and stream thrust along the nozzle inflow boundary. In contrast, cases 5 and 6, which employ mixing enhancement without slots, show reductions in mass flow rate that are likely associated with blockage effects. Due to this geometry dependence in mass flow rates, C_{FG} is preferred over gross thrust as a figure of merit to assess thrust implications of nozzle mixing enhancement. As observed on the bottom row of the table, all enhanced mixing nozzle geometries considered here provide only small reductions in C_{FG} relative to the reference nozzle. The largest C_{FG} reduction of 0.024 is found for the slotted nozzle without VGs (case 4). In comparing propulsive efficiency between the slotted VG nozzle cases with flat and curved VGs, it is found that curved VGs permit a smaller mass flow increase relative to the reference case (6.54% vs. 7.79%) while providing a negligibly higher C_{FG}. As the curved VG nozzle also gives slightly improved high frequency noise reduction (for example, as shown in the table, $\Delta\varphi_{f=2\,\mathrm{kHz}}(x) = 1.8$ dB for case 2 vs. 1.6 dB for case 3) it follows that curved VGs are preferable based on both propulsive and acoustic characteristics.

V. Curved Vortex Generator Design Sensitivities

Results presented in Section IV show both acoustic and propulsive performance advantages for a slotted VG nozzle with curved VGs, in comparison to one with flat VGs or to a slotted nozzle without VGs. Given these results, one next step in a design space exploration is to evaluate design parameter sensitivities and potential improvements associated with geometry variation in the slotted nozzle employing curved VGs. With these goals in mind, seven additional nozzle geometries are introduced in this section. These geometries are displayed in Fig. 14 and are distinguished from earlier geometries and from each other as follows: (2a) has slots that extend to the nozzle lip, and is otherwise identical to 2; (2b) varies from 2 in the fact that all slot/VG pairs are identical, and all VG vortices circulate in the same direction; (2c) is the same as 2 but with the VG profile flattened and extended in the azimuthal direction, in order to reduce both mass flow through the slots and pressure along the slot-side VG surfaces; (2d) is the same as 2c but with the VG planform shape altered (more rectangular, less triangular) in order to increase VG wetted area and to increase slot blockage; (2e) differs from 2 in the use of altered azimuthal spacing between neighboring VG/slot pairs, with uniform spacing based on VG tip (instead of trailing edge root) locations; (2f) is based on 2c but uses the same modification in azimuthal VG spacing as 2e; (2g) varies from 2c only in the extension of slots to the nozzle lip, as in 2a; and (4a) is the same as 4 (slots, no VGs) but with slots that extend to the nozzle lip.

Cumulative source intensities φ_F, as defined by Eq. (5), are plotted at 1, 2 and 4 kHz in Figs. 15 for the seven new cases described above, as well as for the reference nozzle (case 1) and slotted nozzle with curved VGs (case 2) which was analyzed in previous sections. Taking results at all three frequencies into account, the greatest overall cumulative noise reduction at $x/D_{exit} \leq 1$is found for case 2a, where curved VGs are paired with slots that extend to the nozzle lip. For example, in comparison to the reference nozzle case, case 2a provides cumulative noise reductions of 2.6 dB at both 1 kHz and 2 kHz, and 1.0 dB at 4 dB, at no shielding ($x/D_{exit} = 0$) conditions. For a shielding length $x/D_{exit} = 1$, case 2a gives even greater noise reduction differences of 2.8 dB at 1 kHz, 3.5 dB at 2 kHz and 3.6 dB at 4 kHz. Another important observation in Figs. 15 is that, with a few exceptions including cases 2a, 2c and 2g, differences among results for most curved VG cases at $x/D_{exit} \leq 1$are within likely error margins associated with model form uncertainties for the turbulence model and acoustic source model. These uncertainties, which are expected to be on the order of 1 dB, prevent reliable design optimization efforts based on RANS-based tools as used in this study, and indicate the importance of higher fidelity analysis and/or experimental assessment.

Despite the general lack of large variation between results in Figs. 15 for different curved VG nozzle geometries, several design sensitivities can still be observed. One such observation is that the flattening of VGs toward the nozzle inner wall, as distinguishes case 2c from case 2, leads to small reductions in high frequency noise (0.7 dB and 0.3 dB, at 2 kHz and 4 kHz, respectively) for $x/D_{exit} \leq 1$. In results for case 2d, where VG area is increased relative to case 2c, lower frequency noise increases slightly (by 0.2 dB at 1 kHz) in comparison to both 2c and 2, presumably due to increased slot blockage and a resulting decrease in mass flow through the slots. In a comparison of results for $x/D_{exit} \leq 1$ between cases 2 and 2e, and between 2c and 2f, improved noise reduction is found when VGs are spaced such that distances are smaller between neighboring VG vortices that interact to create outward (rather than inward, as in 2e and 2f) streams which impinge on the mixing layer. As only small differences exist between results in Figs. 15 for cases 2 and 2b, it is assumed that there are no substantial advantages at conditions of interest to either the inclusion or exclusion of symmetric slot/VG pairs. As one final observation from these figures, it is found in comparing results from case 4a with those from 2a and 2g that there are considerable acoustic benefits to including VGs in a slotted nozzle for which the slots extend to the nozzle lip. While case 2a and (to a lesser extent) 2g show consistent improvements over the reference nozzle case for $x/D_{exit} \leq 1$, case 4a – where a slotted nozzle is considered without VGs – actually shows a small increase in 4 kHz noise relative to the reference case.

Various propulsive performance metrics are displayed in Table 2 for the cases considered in this section. As a partial indicator of acoustic benefits for each case, cumulative noise reduction values relative to the reference nozzle (case 1) at 2 kHz and $x/D_{exit} = 0$ are also shown in the table. Gross thrust is shown to vary between these cases nearly in proportion to changes in mass flow rate, and therefore only very small differences exist among C_{FG} values. Another finding from results in Table 2 is that, as expected when VGs are flattened and or enlarged to increase blockage of adjacent slots, cases 2c and 2d provide significant reductions in mass flow relative to case 2. In contrast, cases 2a and 4a allow large increases in mass flow following the extension of slots to the nozzle lip. While slots that extend to the nozzle lip may be preferable based on a combination of acoustic and propulsive considerations, following the results in Table 2 and in Figs. 15, it should be noted that that this geometry modification may lead to flutter, aeroelastic resonance, or other stiffness/weight penalties which should be weighed against any potential benefits.

VI. Assessment of Jet Noise Directivity

High frequency noise – roughly 2 kHz and above – is of primary interest in this work due to a combination of factors; these include comparatively high annoyance or objectionability, a related dominant contribution to effective perceived noise level (EPNL) during flyover, and attenuation potential through shielding and/or nearfield mixing enhancement. However, jet noise at much lower frequencies also contributes significantly to EPNL due to high intensity and long duration exposure for a farfield observer at large polar angles. This low frequency noise tends to be generated far downstream of the nozzle, with strong directivity toward the jet axis, and is therefore not amenable to noise reduction via shielding. In order to provide a rough estimation of low frequency directivity effects for the nozzle geometries of interest here, mSrc is used to calculate the power spectral density (PSD) at polar angles of 90º and 150º (representing flyover and down-range locations, respectively) for selected cases. These cases, which are shown in Fig. 16, include the following: (1) the reference axisymmetric nozzle; (2) the baseline slotted VG nozzle with curved VGs; (2a) a modification of case 2 with slots that extend to the trailing edge; (2g) a modification of 2a with VGs that are flatted in profile for increased slot blockage; and (6) the chevron nozzle. PSD calculations are performed in mSrc for an observer located at various polar angles 30 m from the nozzle exit.

PSD plots are presented at 90º and 150º in Figs. 17. At both angles, and for all five cases considered here, the maximum intensity is found at roughly 100-200 Hz. The drop-off on either side of this frequency is particularly sharp at 150º, where an expected low frequency bump is associated with large turbulent structures far downstream of the nozzle. In comparison to the reference nozzle, the chevron nozzle (case 6) shows the greatest low frequency noise reduction at both 90º and (especially) 150º. For example, the chevron nozzle is found to provide a reduction in PSD of approximately 2.0 dB around the 150 Hz peak at 150º. In contrast, for frequencies between 2 kHz and 5 kHz, the chevron nozzle generates significantly more noise than the reference nozzle, whereas all three sets of slotted VG nozzle curves indicate substantial noise reduction.

VII. Throttle Correction to Noise Reduction Estimates

In interpreting noise quantities for nozzle configurations that lead to reduced propulsive efficiency, the desire to maintain takeoff speed and climb rate should be taken into account. More specifically, if jet noise reduction is accompanied by a decrease in thrust, then a higher throttle setting is required to compensate. The resulting increase in jet noise will decrease – and potentially eliminate – any noise reduction. An approximate means to account for this effect is employed here for any given nozzle configuration (j) which as designed to reduce jet noise in comparison to the reference nozzle (1). It is assumed that, to compensate for reduced propulsive efficiency in (j), the average nozzle exit velocity must be increased by a factor that is conservatively estimated to equal the ratio of gross thrust coefficient values $C_{FG(1)}/C_{FG(j)}$. Then, following a standard scaling relation[17] and neglecting any frequency dependence, the cumulative jet noise intensity can be assumed to increase by a factor of $\left(C_{FG(1)}/C_{FG(j)}\right)^8$ on a linear scale. This corresponds to the following additive change in cumulative intensity as given in dB:

$$\Delta\varphi_{(j)} \approx 10log_{10}\left[\left(\frac{C_{FG(1)}}{C_{FG(j)}}\right)^8\right] = -80log_{10}\left(1 + \Delta C_{FG(j)}/C_{FG(1)}\right) \tag{6}$$

where

$$\Delta C_{FG(j)} \equiv C_{FG(j)} - C_{FG(1)}$$

A throttle-corrected noise reduction estimate may then be computed for any case (j) and frequency f by translating the cumulative intensity curve $\varphi_f(x)$ upward by a constant $\Delta\varphi_{(j)}$. For reference, a derivation of Eq. (6) is provided in the appendix.

Throttle-corrected cumulative source intensities at 2 kHz are plotted in Fig. 18 for all nozzle geometries that are shown in 16 and considered above in the analysis of Section VI. One observation from Fig. 18 is that the throttle correction leads to an increase in φ_f of around 0.6-0.7 dB for the slotted VG nozzle cases, whereas a much smaller increase is found for the chevron nozzle case (6) due to the relatively small magnitude of $\Delta C_{FG(6)}$ as presented in Table 2. More importantly, even after the throttle correction, slotted VG nozzles are shown to generate considerably lower noise for f = 2 kHz and $x/D_{exit} \leq 1$ (to the left of the vertical line in Fig. 18) than either the reference nozzle or the chevron nozzle. As an example, for case 2a the 2 kHz throttle-corrected cumulative intensity with no shielding (x/D_{exit}

= 0) is around 1.9 dB lower than the corresponding value for the reference nozzle. It should be emphasized that the throttle correction and the pre-correction noise estimate are subject to large uncertainties associated with several approximations described above and in the appendix. However, it is reasonable to assume from the results in Fig. 18 that the slotted VG nozzle configurations should provide significant high frequency noise reduction, relative to the reference nozzle, even after consideration of propulsive efficiency differences.

VIII. Cruise Performance Assessment

As discussed above in Section I, the main potential advantage of the proposed slotted VG nozzle configuration is the ease of geometry variation – by means of a single moving part – to provide jet noise reduction at takeoff while minimizing propulsive efficiency losses during high speed flight. To this end, cruise performance for this configuration is evaluated in the current section, and slotted VG nozzle characteristics at cruise conditions are compared with those for an axisymmetric reference nozzle and a chevron nozzle. More specifically, supersonic cruise conditions are considered here, and anticipated supersonic nozzle exit conditions are imposed by insertion of a conical plug with a 17.3º half-angle into the convergent nozzle geometries assessed in earlier portions of this study. With the plug in place, convergent nozzles are converted into divergent nozzles with supersonic (choked) inflow conditions and an area ratio of 1.5 between inflow and exit planes. The following cases, denoted with the superscript * to indicate modifications for supersonic cruise, are included in this comparison: (1^*) the reference axisymmetric nozzle with added plug; (2^*) a slotted VG nozzle that differs from case 2 in the addition of a plug and the closure of slots; ($2a^*$) and ($2g^*$) which are similarly distinguished from 2a and 2g, respectively, by the plug and slot closure; and (6^*) a fixed-penetration chevron nozzle (case 6) with added plug. Note that small steps are present along the edges of closed slots in cases 2^*, $2a^*$ and $2g^*$, due to the recession of the slotted ring with respect to nozzle inner and outer surfaces. Furthermore, for cases $2a^*$ and $2g^*$where slots extend to the nozzle lip, the slotted ring trailing edge is positioned a small distance upstream of the nozzle exit plane in order to allow for the ring and nozzle lip to have equal trailing edge thickness of 0.5 cm. All five cruise geometries are displayed in Fig. 19.

Freestream conditions for supersonic cruise analysis include a freestream Mach number of 1.7 and an altitude of 15.2 km, for which the freestream static temperature and pressure are 271 K and 11.06 kPa, respectively. Uniform nozzle inflow conditions are imposed based on generic turbofan cycle calculations, with a total temperature of 569 K, a total pressure of 94.7 kPa and a Mach number of 1.76. Perfectly expanded conditions are assumed at the nozzle exit plane, and hence the exhaust flow is somewhat overexpanded when downstream expansion along the plug surface is taken into account.

In Figs. 20 Mach number contours and streamlines are shown along the centerline plane for cases 1^*, $2a^*$ and 6^* (on the left, center and right, respectively) with purple lines overlaid on the plots to denote sonic conditions. Convergent streamlines are observed in all three plots downstream of the nozzle lip, suggesting over-expanded nozzle flow. In comparison to Mach number contours for cases 1^* and $2a^*$, contours for the chevron plug nozzle (case 6^*) show considerably stronger shock and expansion wave structures between chevron and plug surfaces. These case-specific differences are attributed to the generation of streamwise vortices along the chevron trailing edges, as is expected when chevrons are present under conditions of imperfect expansion. The energy and azimuthal flowfield variation associated with the streamwise vortices are in turn expected to have some adverse impact on propulsive efficiency. Differences in Mach number contours between cases 1^* and $2a^*$ are smaller but still noticeable, and may follow in part from internal nozzle momentum loss in case $2a^*$ due to the additional VG wetted area.

Propulsive efficiency metrics for all five nozzles considered in this section are presented in Table 3. One interesting finding in this table is that little variation exists between gross thrust values at cruise. However, differences between computed net thrust values are nearly an order of magnitude larger; this follows from the fact that, at Mach 1.7 cruise conditions, the ideal nozzle exit velocity is not much larger than the freestream velocity (725 m/s and 561 m/s, respectively) and hence ram drag and gross thrust are comparable. In assessing cruise performance based on the more consequential metric of net thrust, the chevron nozzle is shown to provide a thrust loss of around 6.2%. In contrast, the slotted VG plug nozzle case $2a^*$ allows for a net thrust reduction of only about 0.9% at cruise. For the latter case, the corresponding takeoff geometry is found to reduce 2 kHz unshielded cumulative source intensity by 2.5 dB relative to the reference case, whereas the takeoff geometry (case 6) corresponding to the chevron plug nozzle provides a 2 kHz unshielded source intensity reduction of only 0.8 dB. It should be emphasized, however, that no attempt has been made in this work to adjust chevron penetration or other parameters for an improved balance between cruise efficiency and takeoff noise reduction. Still, the results in Table 3 support the conclusion that, in comparison to a representative fixed-penetration chevron nozzle, the proposed slotted VG nozzle concept does allow for improved balance between cruise and takeoff design objectives.

IX. Summary and Conclusions

A new slotted VG nozzle concept has been presented for jet noise reduction in applications, such as a commercial supersonic transport, where conventional nozzle modifications for takeoff noise reduction may require either complex variable geometry or unacceptable performance degradation during high altitude/high speed flight. The main advantage of the proposed concept, in comparison to other jet mixing enhancement strategies, is the ease with which geometry can be varied based on design requirements during different phases of flight. In particular, a single moving part is used to transition between a geometry favoring mixing enhancement (for takeoff and initial climb) and a geometry favoring propulsive efficiency.

A total of 19 cases were considered here for RANS-based numerical analysis at both takeoff and supersonic cruise conditions. Acoustic analogy calculations were performed to evaluate noise characteristics over a range of frequencies, and a nondimensional parameter based on TKE flow rate derivatives was used to assess turbulent mixing effectiveness. Integrated acoustic source quantities, including cumulative intensities, were employed to estimate the impact of shielding. A new formulation was derived to approximately correct source intensities for any throttle adjustment required to maintain takeoff thrust with respect to a reference nozzle.

In a comparison of several different slotted VG nozzle geometries, the best acoustic results were found for nozzles employing slots that extend to the nozzle lip, with VGs that are curved inward around adjacent slots. In comparison to a reference axisymmetric nozzle, such geometries were shown to provide a 2-3 dB reduction in source intensity at objectionable frequencies in the range of 1-4 kHz. These preferred geometries were subject to an undesirable increase in nozzle mass flow, but only very small penalties were found in gross thrust coefficient. It should be noted that some acoustic benefits were also found for slotted nozzle configurations without VGs. However, the addition of VGs was demonstrated to significantly reduce any takeoff mass flow increase associated with the presence of slots, while providing a considerable reduction in high frequency noise intensities.

A series of calculations were performed to evaluate performance at supersonic cruise conditions, and encouraging results were found for slotted VG nozzle geometries in comparison to a fixed-penetration chevron nozzle. More specifically, a slotted VG configuration with particularly favorable takeoff noise characteristics was determined to reduce net thrust at cruise by about 0.9% relative to a reference axisymmetric nozzle; this compares with a 6.2% net thrust reduction for the chevron nozzle case.

Despite the promising results documented here, several uncertainty sources in computed results limit the extent to which these results can be interpreted in a quantitative and/or absolute sense. These same uncertainty sources also limit the potential for automated design optimization by means of either a surrogate response surface or adjoint methods. Likely dominant contributors to epistemic (reducible) uncertainty include inherent approximations associated with acoustic analogy calculations based on RANS data; a lack of Green's function calculations for noise propagation, including surface reflection, nearfield refraction and atmospheric attenuation effects; and sensitivities to empirically determined turbulence modeling parameters in the RANS calculations. Given these uncertainty sources and the corresponding lack of precision and/or confidence in computed results, an important next step in this work is experimental evaluation. Subscale tests are currently planned in a free jet acoustic test facility at the NASA Glenn Research Center, and a detailed comparison of experimental and computational data is expected. It is hoped that planned tests will promote increased confidence in existing results, while potentially fostering insights into further design improvements.

Appendix: Derivation of Throttle Correction for Source Intensity

For realistic assessment of takeoff jet noise reduction strategies in which acoustic benefits for a modified nozzle are tied to some penalty in propulsive efficiency, estimated noise levels should include adjustments for any increase in throttle required to maintain a desired takeoff speed and climb rate. These adjustments can best be determined by modifying nozzle inflow conditions, based on increased throttle or fuel equivalence ratio, in order to match net thrust to a reference nozzle case. However, an alternate (more easily computed but less accurate) estimate of the throttle-corrected noise impact may be computed by adding a frequency-independent increase $\Delta\varphi$ (in dB) to the noise source intensity, following a simplified edge-case analysis. Such an analysis is provided here.

Three cases are considered based on combinations of nozzle geometry and nozzle inflow conditions. These cases are identified by the following symbols: The subscript (1) denotes the reference nozzle geometry and corresponding inflow conditions. The subscript (j) denotes a modified nozzle geometry designed for jet noise reduction. The superscript *, used with the subscript (j), indicates nozzle inflow conditions for which the throttle is increased to match

net thrust for the reference case. (When the subscript (j) is used without the superscript * then reference inflow conditions are used.)

As a first step in deriving an expression for $\Delta\varphi$, it is assumed that noise intensity scales roughly with the eighth power of the ideal nozzle exit velocity V_{exit} for quasi-one-dimensional isentropic expansion, based on the power law formulation of Lighthill.[17] Thus,

$$\Delta\varphi_{(j)} \equiv \varphi^*_{(j)} - \varphi_{(j)} \approx 10log_{10}\left(\left(V^*_{exit(j)}/V_{exit(j)}\right)^8\right) \tag{A.1}$$

The following simplifying approximations are used here along with Eq. (A.1):

$$C^*_{FG(j)} \approx C_{FG(j)} \tag{A.2}$$

$$P^*_{exit(j)} \approx P_{exit(j)} \approx P_{exit(1)} \approx P_\infty \tag{A.3}$$

$$V_{exit(j)} \approx V_{exit(1)} \tag{A.4}$$

Here C_{FG} is the gross thrust coefficient, P_{exit} is the nozzle exit pressure for quasi-one-dimensional expansion, and P_∞ is the freestream pressure. Based on (A.3) and an additional approximation that the fuel mass contribution may be neglected in the mass flow $\dot{m}$ through the nozzle, the net thrust can be computed as

$$F_{net} = C_{FG}\dot{m}V_{exit} - \dot{m}V_\infty \tag{A.5}$$

Two limiting cases are considered in this analysis: a static case with a freestream Mach number $M_\infty = 0$ and a transonic case with $M_\infty \approx 1$.

For the first case, at static (uninstalled engine) conditions, an additional approximation is imposed that

$$\rho^*_{exit(j)} \approx \rho_{exit(j)} \approx \rho_{exit(1)} \tag{A.6}$$

where ρ_{exit} is the exit density in an isentropically expanding nozzle. (Note that, in representative turbofan cycle calculations at $M_\infty = 0$ using a wide range of throttle settings, exit density was found to vary by no more than roughly 1%.) By equating net thrust at static conditions, it can be shown that

$$C_{FG(j)}\dot{m}^*_{(j)}V^*_{exit(j)} = C_{FG(1)}\dot{m}_{(1)}V_{exit(1)} \tag{A.7}$$

hence

$$\frac{V^*_{exit(j)}}{V_{exit(1)}} = \frac{C_{FG(1)}}{C_{FG(j)}}\frac{\dot{m}_{(1)}}{\dot{m}^*_{(j)}} \tag{A.8}$$

Next, (A.6) is used to find the following approximation relating mass flow rates:

$$\frac{\dot{m}_{(1)}}{\dot{m}^*_{(j)}} \approx \frac{V_{exit(1)}}{V^*_{exit(j)}} \tag{A.9}$$

Substitution of (A.9) into (A.8) then gives

$$\left(\frac{V^*_{exit(j)}}{V_{exit(1)}}\right)^2 \approx \frac{C_{FG(1)}}{C_{FG(j)}} \tag{A.10}$$

Thus, from Eqs. (A.1) and (A.10), it is found that

$$\Delta\varphi_{(j)} \approx 10log_{10}\left[\left(\frac{C_{FG(1)}}{C_{FG(j)}}\right)^4\right] = -40log_{10}\left(1 + \Delta C_{FG(j)}/C_{FG(1)}\right) \tag{A.11}$$

where

$$\Delta C_{FG(j)} \equiv C_{FG(j)} - C_{FG(1)}$$

For the second limiting case of transonic flight, where $M_\infty \approx 1$, (A.3) is employed to equate net thrust between throttle corrected and reference nozzle cases:

$$C^*_{FG(j)}\dot{m}^*_{(j)}V^*_{exit,ideal(j)} - \dot{m}^*_{(j)}V_\infty = C_{FG(1)}\dot{m}_{(1)}V_{exit,ideal(1)} - \dot{m}_{(1)}V_\infty \tag{A.12}$$

An approximation

$$\dot{m}^*_{(j)} \approx \dot{m}_{(j)} \approx \dot{m}_{(1)} \tag{A.13}$$

follows from the above assumption that fuel mass flow contributes negligibly to the mass flow rate $\dot{m}$ through the nozzle. When substitutions based on (A.2) and (A.13) are performed in (A.12), the following relation is found between nozzle exit velocities:

$$\frac{V^*_{exit(j)}}{V_{exit(1)}} = \frac{C_{FG(1)}}{C_{FG(j)}} \tag{A.14}$$

Substitution of (A.14) into (A.1) then gives

$$\Delta\varphi_{(j)} \approx 10log_{10}\left[\left(\frac{C_{FG(1)}}{C_{FG(j)}}\right)^8\right] = -80log_{10}\left(1 + \Delta C_{FG(j)}/C_{FG(1)}\right) \tag{A.15}$$

At typical takeoff conditions between $M_\infty = 0.2$ and $M_\infty = 0.3$, the actual throttle-corrected noise increase $\Delta\varphi$ is assumed to be bounded by estimates for the static and transonic cases. The transonic case expression (A.15) is shown to provide a more conservative (i.e. larger) estimate for the required throttle correction than the static case expression (A.11), and (A.15) is therefore used to determine an approximate upper bound for additional noise associated with any throttle increase needed to compensate for reduced nozzle efficiency.

Acknowledgments

The author would like to acknowledge Jonathan Seidel and James Bridges at NASA Glenn Research Center for a series of valuable discussions and suggestions which have helped to guide the work presented here. This work has been supported by the NASA Commercial Supersonic Technology Project.

References

[1]Goodykoontz, J., "Effect of a Semi-Annular Thermal Acoustic Shield on Jet Exhaust Noise," NASA TM-81615, 1980.

[2]Lord, W. K., Jones, C. W., and Stern, A. M., "Mixer Ejector Nozzle for Jet Noise Suppression," AIAA paper 90-1909, 1990.

[3]Schum, E. J., and Dehart, J. H., "Ejector Nozzle Development," *International Council of the Aeronautical Sciences*, ICAS-82-4.3.3, 1982.

[4]Tew, D. E., Teeple, B. S., and Waitz, I. A., "Mixer-Ejector Noise-Suppressor Model," *Journal of Propulsion and Power*, Vol. 14, No. 6, pp. 941-949, 1998.

[5]Berton, J. J., "Noise Reduction Potential of Large, Over-the-Wing Mounted, Advanced Turbofan Engines," NASA TM-2000-210025, 2000.

[6]Zaman, K. B. M. Q., Reeder, M. F., and Samimy, M., "Control of an Axisymmetric Jet using Vortex Generators," *Physics of Fluids*, Vol. 6, No. 2, pp. 778-793, 1994.

[7]Rogers, C. B., and Parekh, D. E., "Mixing Enhancement by and Noise Characteristics of Streamwise Vortices in an Air Jet," *AIAA Journal*, Vol. 32, No. 3, pp. 464-471, 1994.

[8]Surks, P., Rogers, C. B., and Parekh, D. E., "Entrainment and Acoustic Variations in a Round Jet from Introduced Streamwise Vorticity," *AIAA Journal*, Vol. 32, No. 10, pp. 2108-2110, 1994.
[9]Carletti, M. J., Rogers, C. B., and Parekh, D. E., "Parametric Study of Jet Mixing Enhancement by Vortex Generators, Tabs, and Deflector Plates," *Proceedings of the 1996 ASME Fluids Engineering Division Summer Meeting*, pp. 303-333, 1996.
[10]Birch, S. F., Lawler, J. A., and Paynter, G. C., "Vortex Generators for Internal Mixing in a Turbofan Engine," U.S. Patent 4175640, 1979.
[11]Bray, T. P., *A Parametric Study of Vane and Air-Jet Vortex Generators*, PhD Thesis, Cranfield University, 1998, pp. 30-55.
[12]Burt, J. M., Seidel, J., and Leib, S., "Assessment of Mixer-Ejector Nozzle with Thermal Acoustic Shield for Jet Noise Reduction," AIAA paper 2019-3018, 2019.
[13]Dippold, V. F., "Generating a Grid for Unstructured RANS Simulations of Jet Flows," AIAA paper 2018-3223, 2018.
[14]Biedron, R. T., Carlson, J.-R., Derlaga, J. M., et al., "FUN3D Manual: 13.2", NASA TM-2017-219661, 2017.
[15]Bridges, J., "mSrc Technical and User's Manual, Version 3.5," NASA Glenn Research Center, 2017.
[16]Alkislar, M. B., Krothapalli, A., and Butler, G. W., "The Effect of Streamwise Vortices on the Aeroacoustics of a Mach 0.9 Jet," *Journal of Fluid Mechanics*, Vol. 578, pp. 139-169, 2007.
[17]Lighthill, M. J., "On Sound Generated Aerodynamically II. Turbulence as a Source of Sound," *Proceedings of the Royal Society A*, Vol. 222, No. 1148, 1954, pp. 1-32.

Table 1. Takeoff thrust and propulsive efficiency quantities for geometries in Fig. 2.

Case ID	1	2	3	4	5	6
Case description	reference nozzle	slots, curved 0° VGs	slots, flat 0° VGs	slots, no VGs	15° VGs	chevrons
Cumulative source intensity difference at 2 kHz, $x/D_{exit} = 0$ relative to reference nozzle case	N/A	1.8 dB	1.6 dB	1.3 dB	0.2 dB	0.8 dB
Fractional change in gross thrust relative to reference nozzle case	N/A	4.52%	5.53%	5.60%	-1.86%	-5.94%
Fractional change in net thrust relative to reference nozzle case	N/A	3.98%	4.92%	4.90%	-2.04%	-5.98%
Fractional change in mass flow rate relative to reference nozzle case	N/A	6.54%	7.79%	8.19%	-1.20%	-5.79%
Gross thrust coefficient C_{FG}	0.992	0.973	0.971	0.968	0.985	0.990
ΔC_{FG} relative to reference nozzle case	N/A	-0.019	-0.021	-0.024	-0.007	-0.002

Table 2. Takeoff thrust and propulsive efficiency quantities for geometries in Fig. 14.

Case ID	1	2	2a	2b	2c	2d	2e	2f	2g	4a
Case description	ref. nozzle	slots, curved 0° VGs	slots to trailing edge	identical slot/VG pairs	flatter VG profile vs. 2	larger VG area vs. 2c	altered spacing vs. 2	altered spacing vs. 2c	like 2c, slots to trailing edge	no VGs, slots to trailing edge
Cumulative source intensity difference at 2 kHz, $x/D_{exit} = 0$ relative to reference nozzle case	N/A	1.8 dB	2.5 dB	1.9 dB	2.0 dB	1.9 dB	1.5 dB	1.8 dB	2.2 dB	1.2 dB
Fractional change in gross thrust relative to reference nozzle case	N/A	4.52%	5.42%	4.92%	3.94%	3.48%	4.58%	3.98%	4.62%	7.05%
Fractional change in net thrust relative to reference nozzle case	N/A	3.98%	4.93%	4.39%	3.44%	2.93%	4.03%	3.47%	4.17%	6.53%
Fractional change in mass flow rate relative to reference nozzle case	N/A	6.54%	7.21%	6.89%	5.80%	5.49%	6.63%	5.85%	6.29%	8.99%
Gross thrust coefficient C_{FG}	0.992	0.973	0.975	0.974	0.974	0.973	0.973	0.974	0.976	0.974
ΔC_{FG} relative to reference nozzle case	N/A	-0.019	-0.017	-0.018	-0.017	-0.019	-0.019	-0.018	-0.016	-0.018

Table 3. Takeoff thrust and propulsive efficiency quantities for geometries in Fig. 19.

Case ID	1*	2*	2a*	2g*	6*
Case description	reference plug nozzle	closed slots, curved 0° VGs	slots to trailing edge	flattened VG profile, slots to trailing edge	plug nozzle with chevrons
Cumulative source intensity difference at 2 kHz, $x/D_{exit} = 0$ relative to reference nozzle case	N/A	1.8 dB	2.5 dB	2.2 dB	0.8 dB
Fractional change in gross thrust relative to reference nozzle case	N/A	-0.42%	-0.12%	-0.11%	-0.82%
Fractional change in net thrust relative to reference nozzle case	N/A	-3.13%	-0.92%	-0.86%	-6.17%
Fractional change in mass flow rate relative to reference nozzle case	0.866	0.863	0.865	0.865	0.859
Gross thrust coefficient C_{FG}	N/A	-0.004	-0.001	-0.001	-0.007
ΔC_{FG} relative to reference nozzle case	N/A	1.8 dB	2.5 dB	2.2 dB	0.8 dB

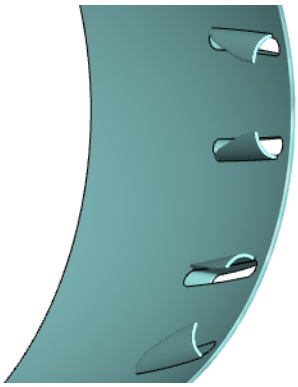

Figure 1. Partial view of slotted VG nozzle.

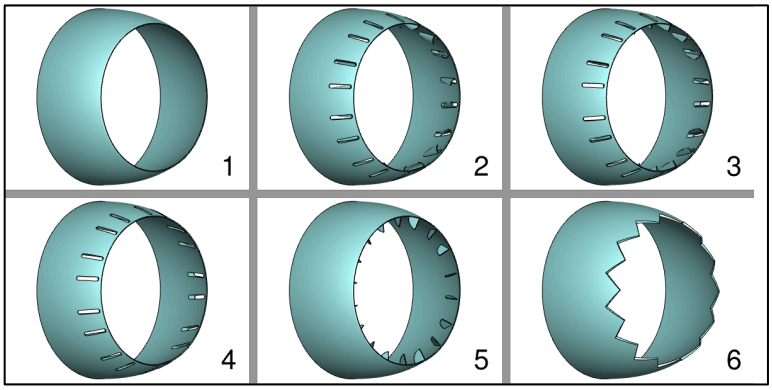

Figure 2. Nozzle geometries used in initial comparison.

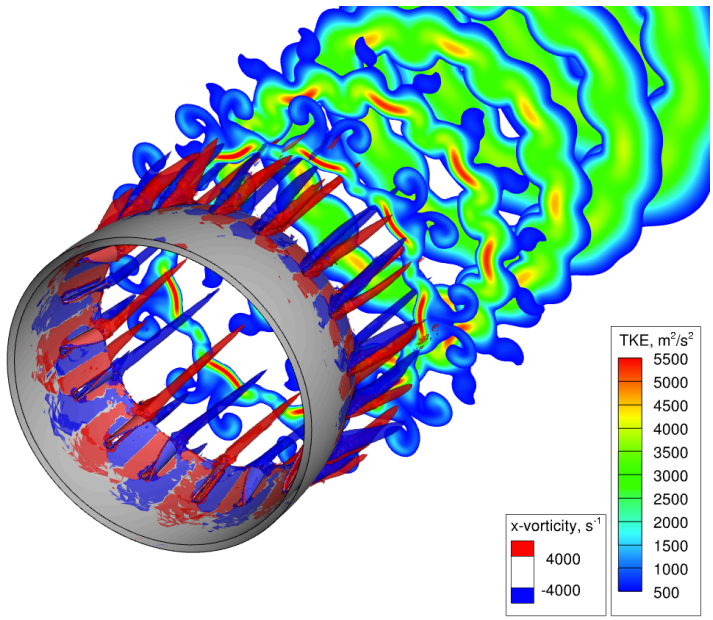

Figure 3. Isometric view of TKE along transverse planes, with iso-contour surfaces of *x*-directed vorticity.

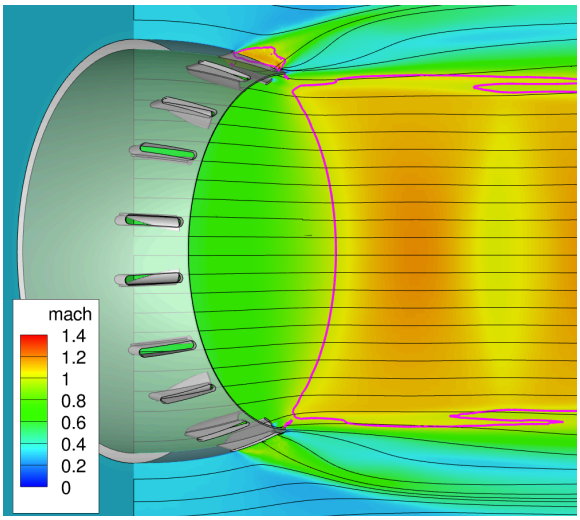

Figure 4. Centerline Mach number contours and streamlines. Sonic conditions are indicated by purple lines.

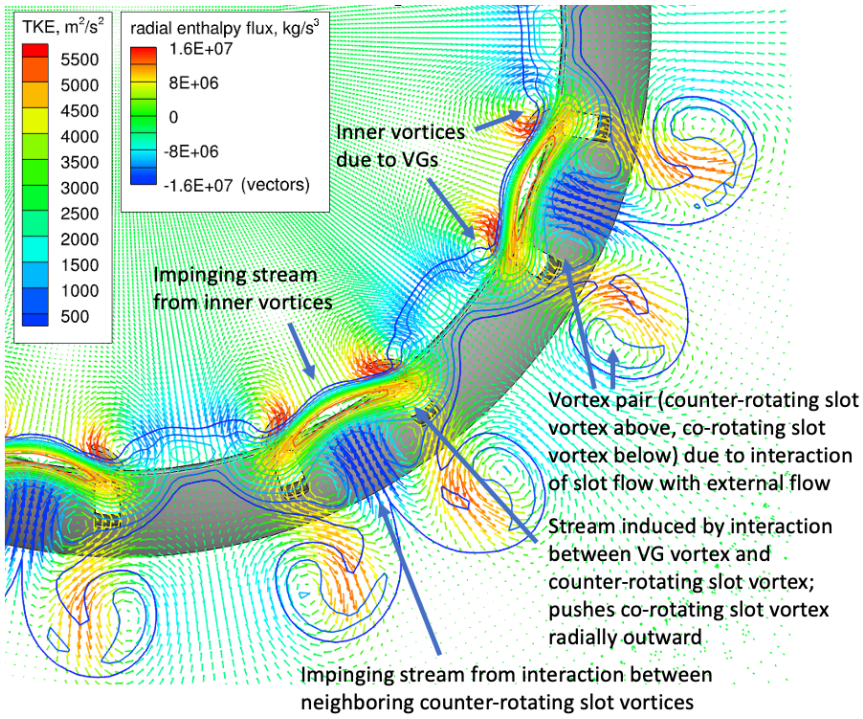

Figure 5. Iso-contour lines for TKE and velocity vectors along a transverse plane at x/D_{exit} = 0.5. Vectors are colored according to radial flux of total enthalpy.

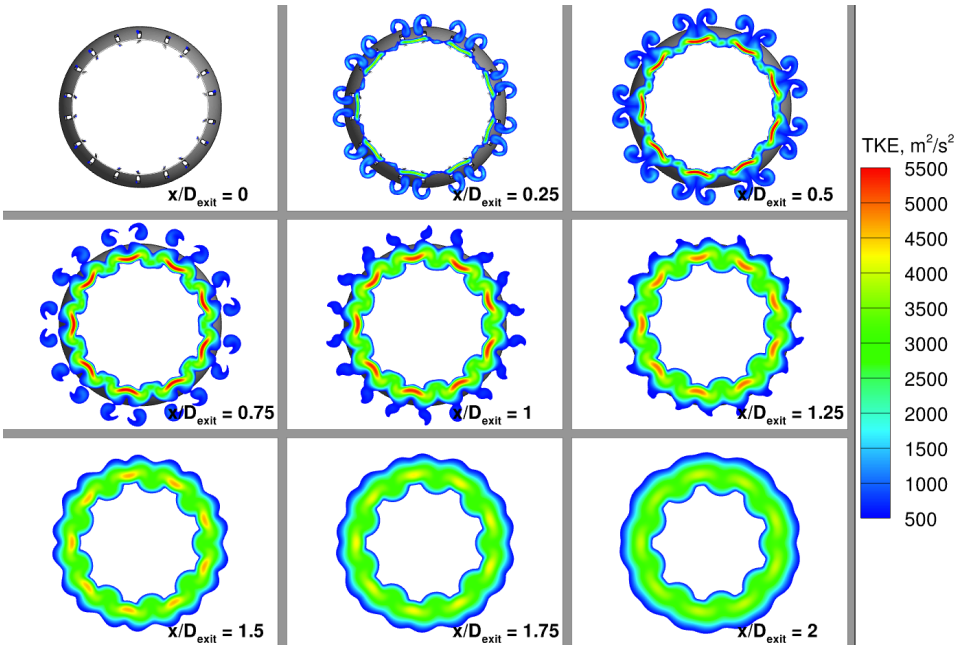

Figure 6. TKE contours along transverse planes (x/D_{exit} = 0, 0.25, 0.5, …).

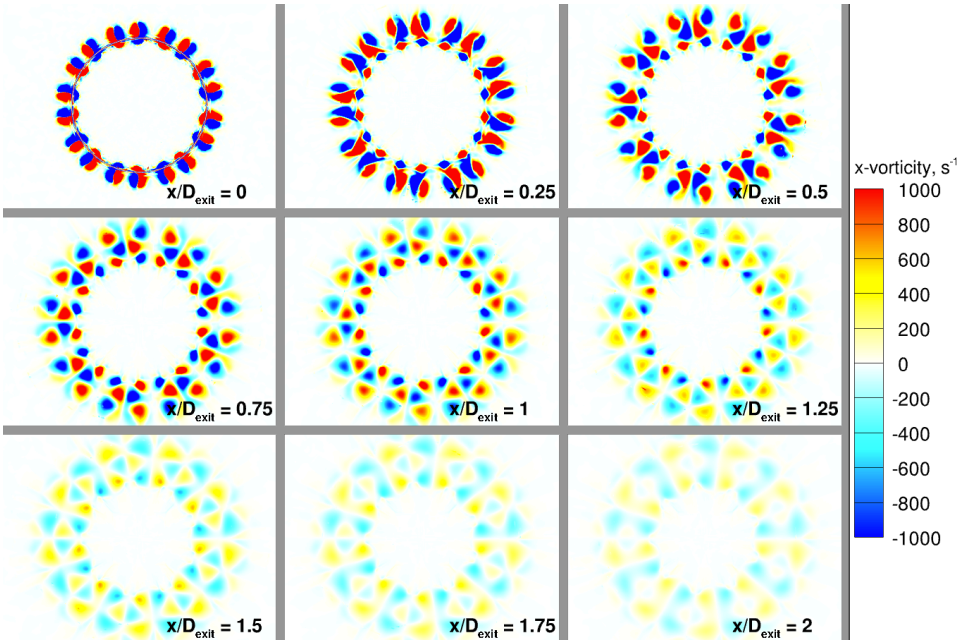

Figure 7. Contours of *x*-vorticity along transverse planes.

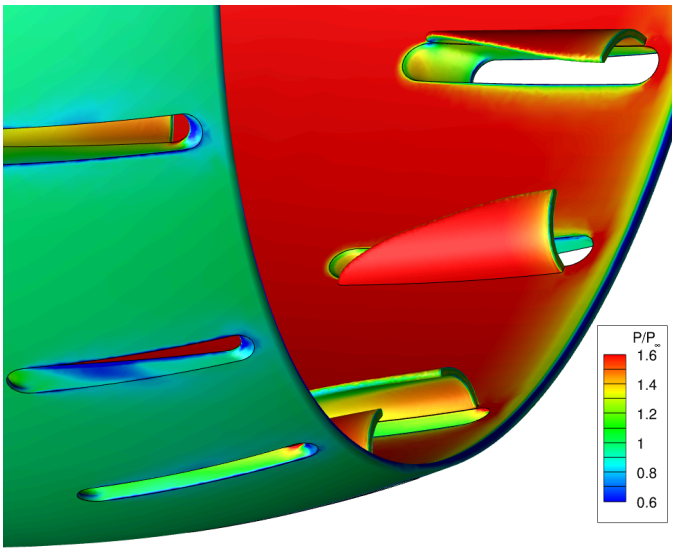

Figure 8. Contours of surface pressure.

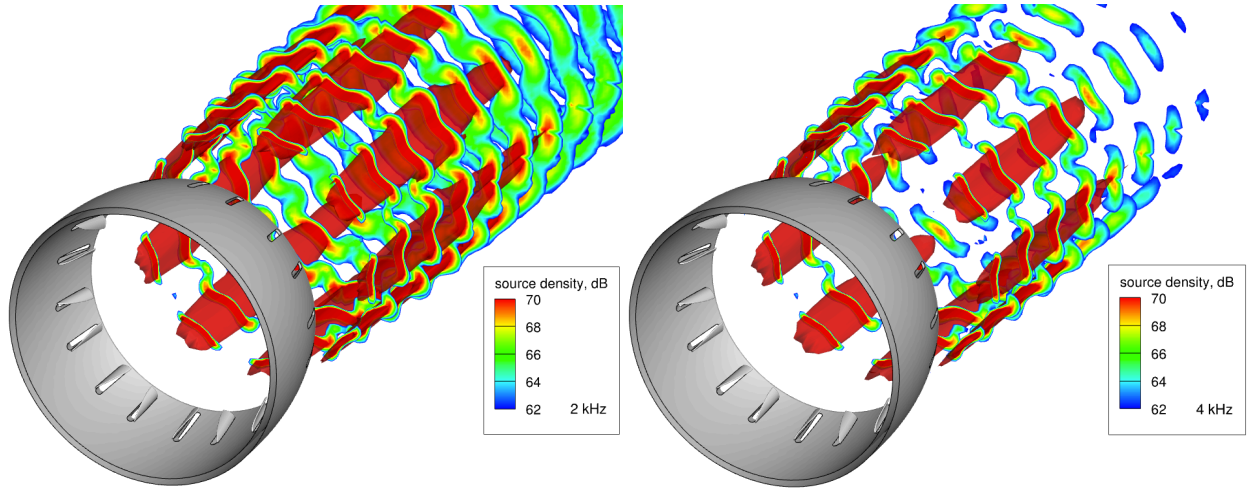

(a) **(b)**

Figures 9. Contours of source density at (a) 2 kHz and (b) 4 kHz. Iso-contour surfaces are displayed at 70 dB, and slices are shown along transverse planes (x/D_{exit} = 0, 0.5, 1, …).

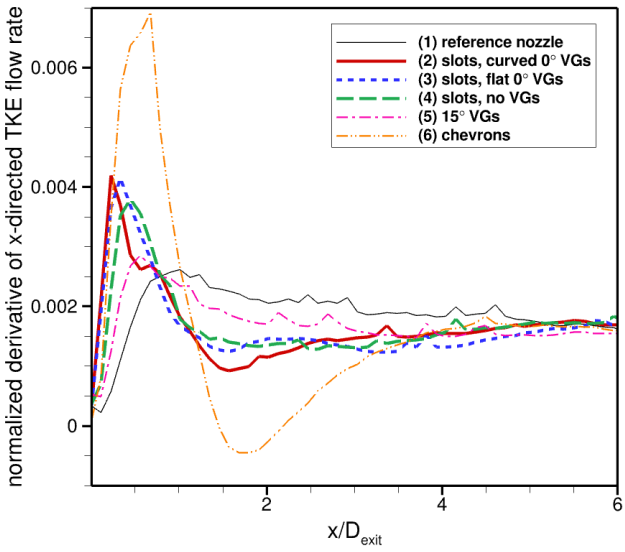

Figure 10. Variation in mixing rate parameter with x/D_{exit}.

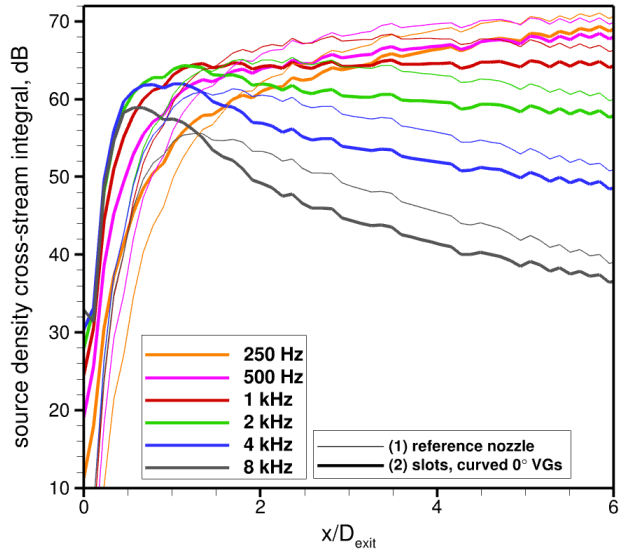

Figure 11. Source density cross-stream integral for frequencies between 250 Hz and 8 kHz.

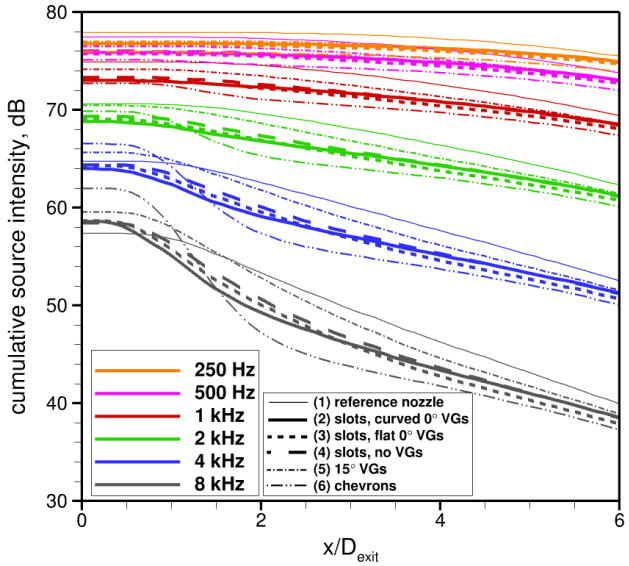

Figure 12. Cumulative source intensity at various frequencies over the interval [*x*, ∞).

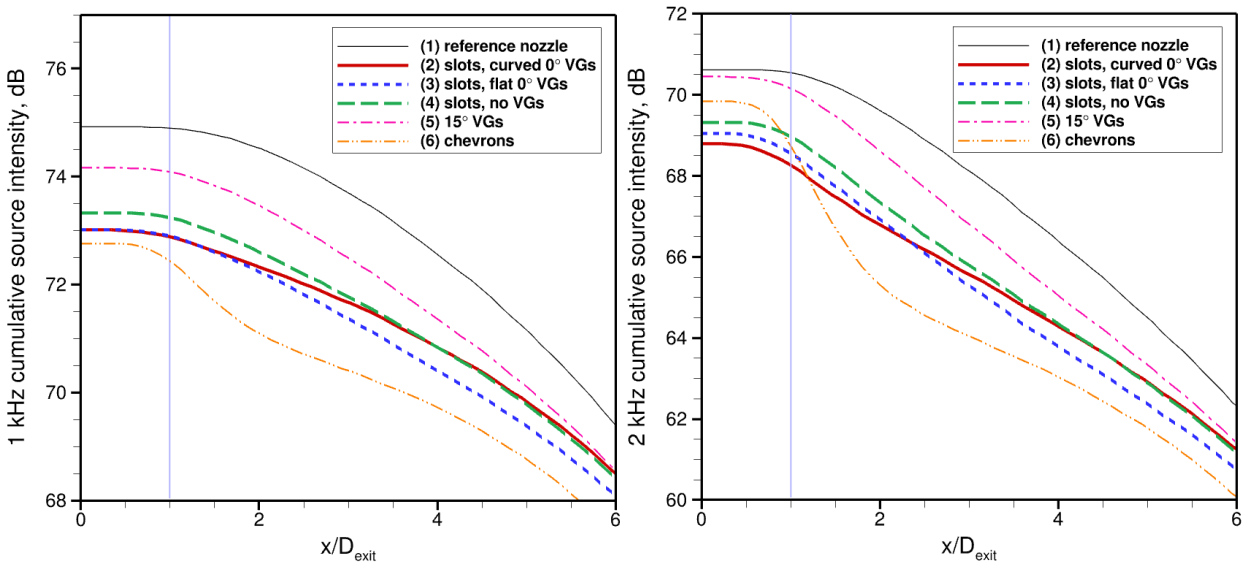

(a) **(b)**

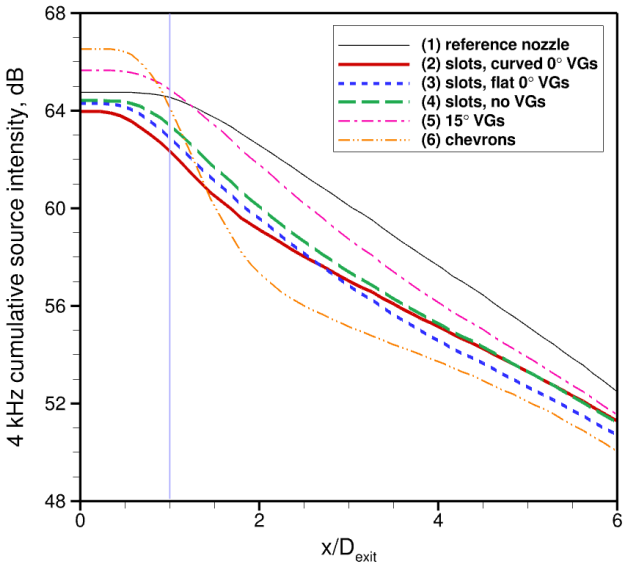

(c)

Figures 13. Cumulative source intensity over [*x*, ∞) at (a) 1 kHz, (b) 2 kHz and (c) 4 kHz.

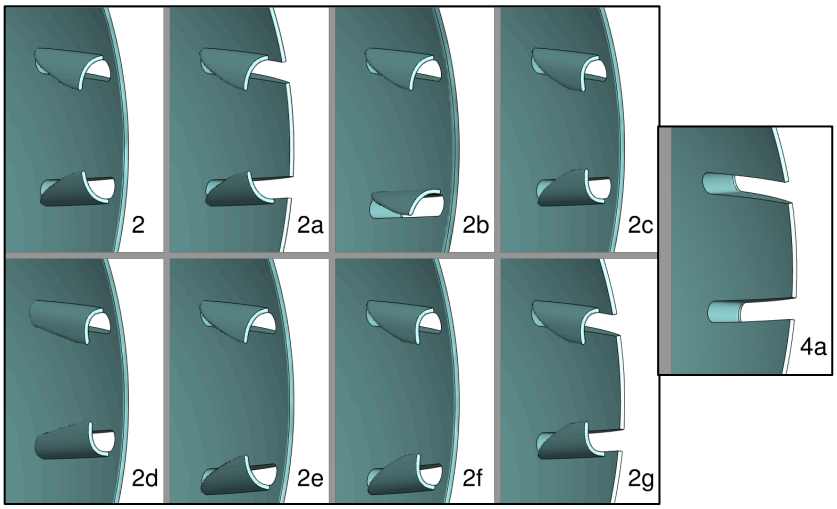

Figure 14. Geometries considered in sensitivity analysis for curved VG/slotted nozzle design.

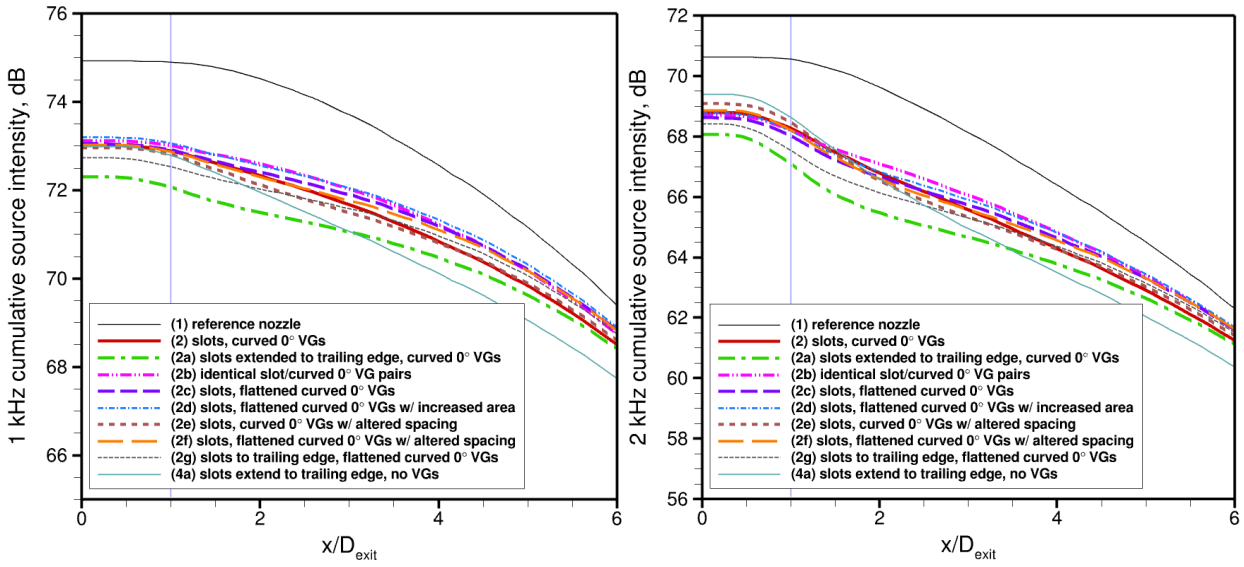

Figures 15. Cumulative source intensity for geometries displayed in Fig. 14 at (a) 1 kHz, (b) 2 kHz and (c) 4 kHz.

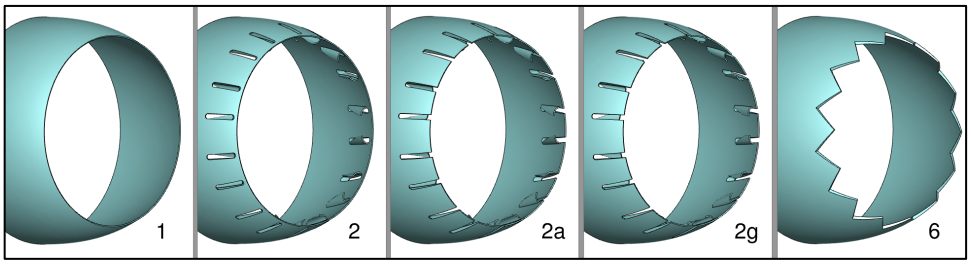

Figure 16. Geometries considered in assessment of source directivity.

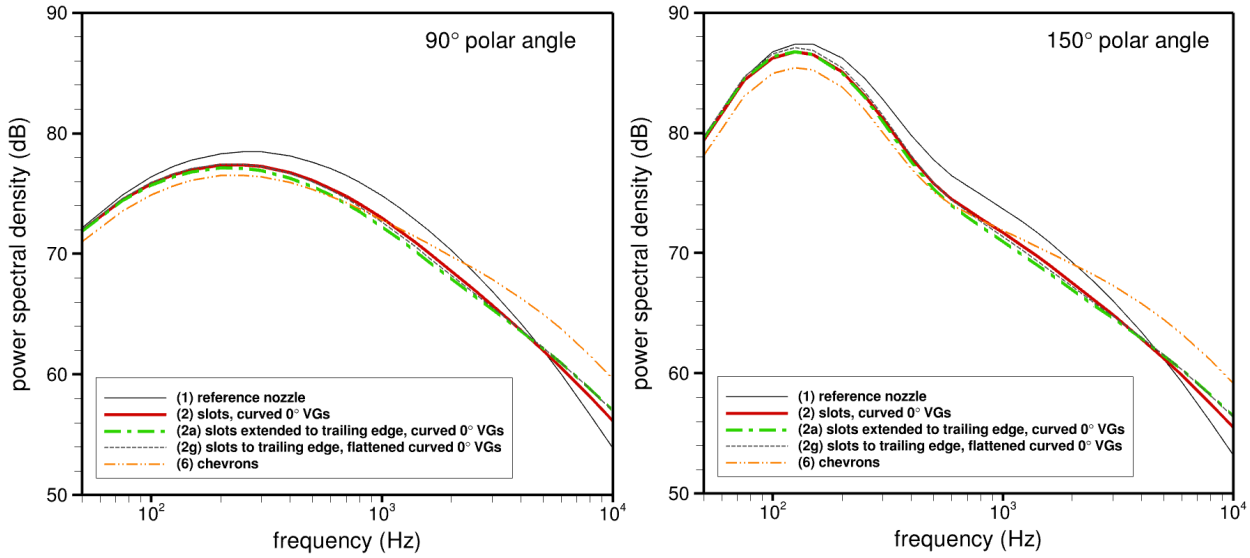

Figures 17. Power spectral density at farfield polar angles of (a) 90° and (b) 150°.

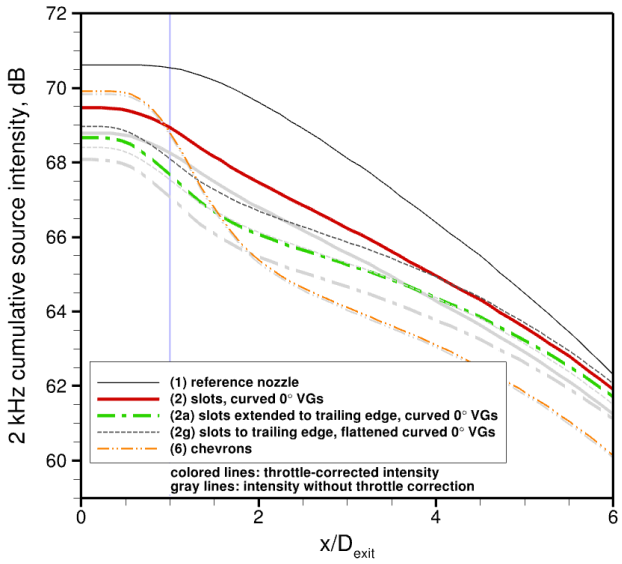

Figure 18. Cumulative source intensity at 2 kHz, with and without throttle correction.

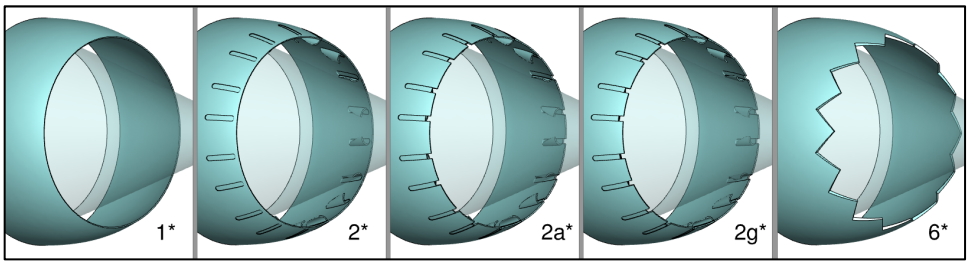

Figure 19. Geometries used for cruise performance evaluation.

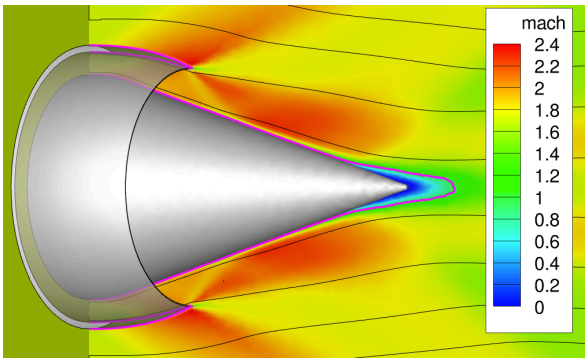

(a)

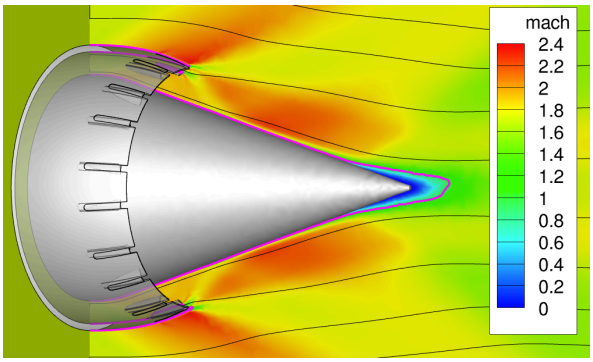

(b)

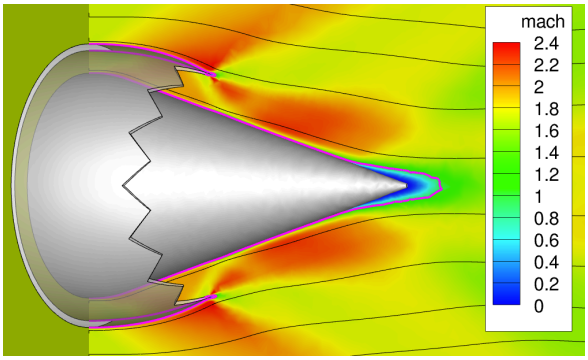

(c)

Figures 20. Streamlines and Mach number contours along centerline plane for cases (a) 1^*, (b) $2a^*$ and (c) 6^*.